Research Square

Preprints are preliminary reports that have not undergone peer review.
They should not be considered conclusive, used to inform clinical practice,
or referenced by the media as validated information.

Active throttling and dual-thrust capability of 3D-printed swirl-star fuel grains for hybrid rocket engines

Mostafa El-Naggar
Military Technical College
Ahmed F. A. Hassan
a.farid@mtc.edu.eg

Military Technical College
Mahmoud Y. M. Ahmed
Military Technical College
Anwer Hashish
Military Technical College

Article

Keywords:

Posted Date: June 29th, 2026

DOI: https://doi.org/10.21203/rs.3.rs-9992285/v1

License: This work is licensed under a Creative Commons Attribution 4.0 International License.
Read Full License

Additional Declarations: No competing interests reported.

Version of Record: A version of this preprint was published at Scientific Reports on October 5th, 2026.
See the published version at https://doi.org/10.1038/s41598-026-71259-x.

Active throttling and dual-thrust capability of 3D-printed swirl-star fuel grains for hybrid rocket engines

Mostafa El-Naggar[1], Ahmed F. A. Hassan[2,*], Mahmoud Y. M. Ahmed[2], Anwer Hashish[2]

[1] 1 PhD student, Department of Aerospace Engineering, Military Technical College, Egypt.
[2] 2 Associate Professor, Department of Aerospace Engineering, Military Technical College, Egypt.
[*] Corresponding author. a.farid@mtc.edu.eg

Abstract

Throttling capability and dual-thrust (boost–sustain) operation are essential features of modern propulsion systems for orbital maneuvering, planetary descent and guided missiles applications. Hybrid rocket Hybrid rocket Motors inherently have thrust modulation by changing the oxidizer flow but fast stable throttling is often limited because of the non-linear, unstable regression behaviour of conventional fuel grains. This study explores additively star swirl reverse port geometries combined molded acrylonitrile butadiene styrene (ABS) fuel grains with a swirl injector, with a view to realizing responsive dual-thrust operation with low oscillation. Overall of 66 static fire tests (60 steady state and 6 dedicated active throttling experiments) were conducted to quantify the transient response and steady state regression characteristics of grains with N=5, 7 and 9 star points. Empirical Regression-rate laws have been developed for tubular and swirl-star configurations in a modified 1-inch motor. Findings show that the 5-point swirl-star-reverse (5SSR) grain yields the highest regression rate and minimum pressureundershootwithrapidstabilisationduringstep-wiseoxidizerflowreductionfrom5 to 2.5 g/s. This arrangement clean boosts, with transitions from boost to sustain producing average pressure fluctuations of less than 5% providing greater dynamic response. the mean, pointing to a better dynamic behavior. Additive manufacturing with optimized swirl geometry, and an exponent approaching unity offers a tractable route to programmable hybrid propulsion systems capable of performing complex thrust profiles for future aerospace missions.

---

1 Introduction

Hybrid rocket motors (HRMs) offer the safety and storability of solid propulsion with the throttling and restart capability of liquid systems. However, the practical implementation of these advantages is often limited by the non-linear, diffusion-limited combustion behavior of conventional polymeric fuels [1, 2, 3, 4]. An attractive feature of this work is the need for fast, repeatable transitions between high-thrust boost and low-thrust sustain phases. This is a key capability for planetary landers, divert attitude control systems, and multi-pulse orbital transfer vehicles, which in turn requires a fuel grain with a regression rate $\dot{r} = aG_{\mathrm{ox}}^{n}$ that approaches a linear dependence on oxidizer mass flux G_{ox} ($n \rightarrow 1$) [5, 6]. The coupling between oxidizer flow and fuel gasification is improved with increasing the exponent n, and mixture ratio excursions are reduced during throttling, but thermal lag can never be completely eliminated. A classical example is the turbulent boundary-layer combustion theory of Marxman and Gilbert [7] which predicts an exponent $n \approx 0.5$-0.8. Here a 50

Recent studies show that swirl-augmented grains can significantly increase the regression exponent. Liu et al. [15] observed a 191% increase in the regression rate with an integrated star-swirl grain with a swirl injector, and Heydari et al. [16] obtained $\dot{r} = 0.14\, G_{\mathrm{ox}}^{1.40}$ for swirling oxidizer injection into HTPB. Funami et al. [17] and Takano et

al. [18] showed that star-fractal swirl ports can achieve record-breaking flight altitudes. Wang et al. [19] proposed swirl-radial-injection composite grains to reduce front-end ablation. Together these studies show that a high exponent n can be reached but they have not systematically investigated the transient behaviour of such grains under active modulation of the flow. In ref. The hybrid rocket efficiency is maximized by combining a swirl injector with a reverse swirl star port [20]. The injector creates a rapid swirled flow that enhances the burning of the fuel. The star channels guide this turbulence into stable vortices along the chamber for optimal combustion.

Parallel advances in throttling hardware have further expanded the operational envelope of hybrids. Whitmore and Walker [21] presented an 8-bit digital throttle with parallel solenoid valves on GOX/ABS motors with accurate step, ramp and sinusoidal thrust profiles. Variable-area cavitating venturis were used for deep throttling with low complexity by Ruffin et al. [22], while Dinesh et al. [23] demonstrated passive dual-thrust modulation using multi-layered tubular grains. The key to all these efforts is the need for the fuel grain to have a well-defined, low-lag response to oxidizer flow changes, a property that is highly dependent on the n exponent and the internal ballistics of the grain [24, 25]. In addition, the choice of fuel material and additive manufacturing parameters strongly affect regression behaviour; for example, it has been demonstrated that copper-infused ABS increases regression rates by up to 40% [26] and predictive models for various fuel combinations are still in development for design tools [27].

The purpose of this work is to increase the regression rate of hybrid rocket motors using additively manufactured fuel grains with complex 3D geometries. The present work studies the transition from the initial tubular grains (TB) to more complex star-shaped grains, i.e. basic star (BS), swirl star (SS) and swirl-star-reverse (SSR) with different number of star points (N = 5, 7, and 9), combined with a tangential swirl injector to improve the convective heat transfer and the oxidizer–fuel mixing. Furthermore, the active throttling ability of the optimized grain geometries and their dual-thrust (boost-sustain) performance are evaluated for responsive, low-oscillation thrust modulation for advanced propulsion applications requiring precise trajectory control such as planetary landers, orbital transfer vehicles and guided missiles.

The paper is organised as follows: the experimental methodology, including the solid fuel grain, test motors and injectors, the test setup and throttling mechanism (throttling architecture, sequencing and valve logic), the instrumentation and data acquisition system, test matrix and data reduction methodology; the results and discussion, including the experimental results, steady-state regression behaviour, the throttling effect at N = 5, 7 and 9, the effect of throttling transition time and implications for throttlable hybrid propulsion systems; and the conclusion, summarising the main outcomes of this investigation.

2 Experimental Methodology

2.1 Solid Fuel Grain

Acrylonitrile–Butadiene–Styrene (ABS) was chosen as the solid fuel due to its low cost, wide availability, and excellent processability using additive manufacturing. ABS easily accepts metallic or energetic additives to improve the combustion performance and exhibits a stable and repeatable burning behaviour with gaseous oxygen. The empirical formula of ABS, based on typical monomer ratios, is approximately $C_9H_{11}N$ (rounded for simplicity), with a standard heat of formation of $\Delta H_f^\circ = 62.63\ \mathrm{J\,g^{-1}}$.

Two types of grains were used: tubular and star grains. The star grain design had three variants: basic star, swirl star, and swirl star reverse. The star grain geometry is characterised by seven parameters, among which the number of star points (N) is a key factor. Values of N = 5, 7, and 9 were investigated (Figure 1), which illustrates the grain designs.

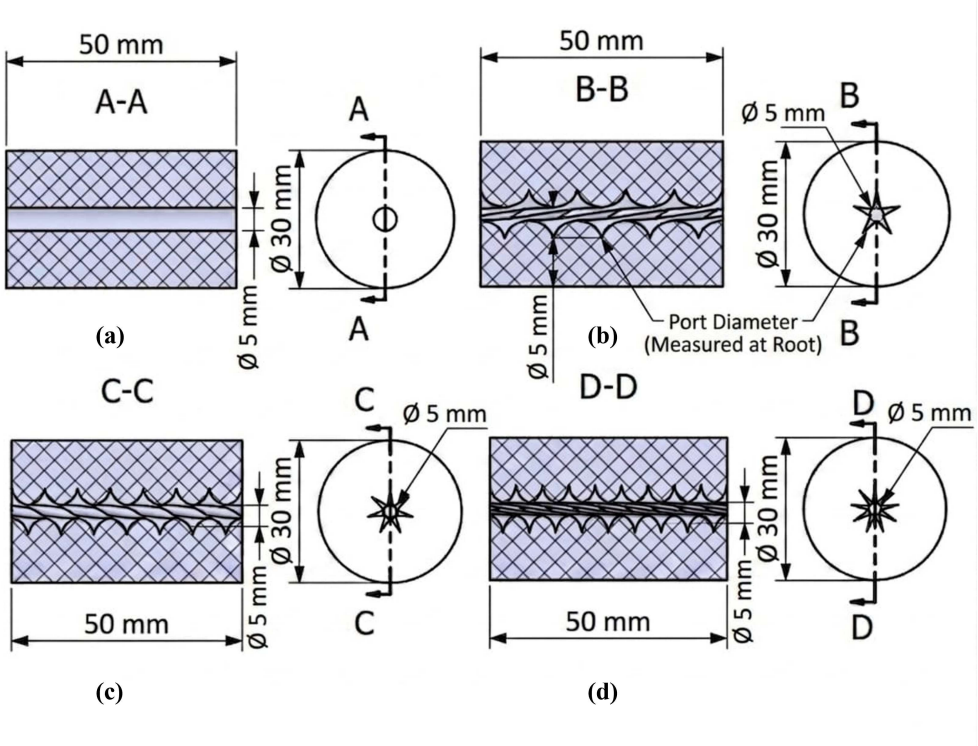


Figure 1: Grain types: (a) tubular, (b) swirl-star with $N = 5$, (c) swirl-star with $N = 7$, and (d) swirl-star with $N = 9$. The cross-sectional views illustrate the star-point geometry and swirl channels.

The fuel grains were fabricated using a Prusa i3 MK3 [33] printer with ABS filament. The printing parameters are listed in Table 1. After being printed, grains were transition fitted into a tubular metal case. The material density of the printed ABS was measured as 1.04 $\mathrm{g\,cm^{-3}}$.

Table 1: 3D printing parameters for ABS grains [34, 35, 36].

Parameter	Value
Nozzle temperature	230°C
Bed temperature	105°C
Infill	100%
Layer height	0.15 mm
Lamination pitch	0.254 mm
Outer diameter	30 mm
Length	50 mm
Initial port diameter	4.86 mm (nominal)

2.2 Test Motors and Injectors

A standard 1-inch test motor was adapted for hybrid combustion testing (Figure 2). The forward closure was modular to accommodate various swirl injector geometries and included a port for pressure measurement with pre- and post-combustion chamber lengths of 15 mm and 28 mm, respectively.

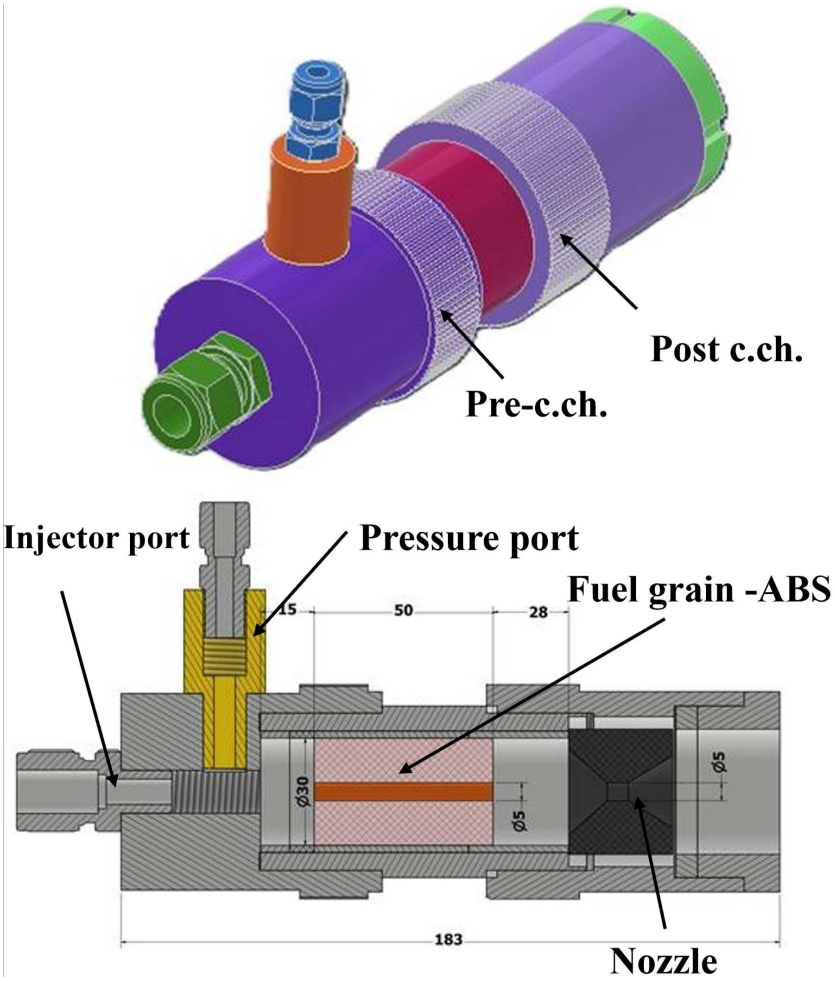


Figure 2: One-inch test motor assembly.

In this study a single type of injector, a swirl injector, was used which was designed to impart a tangential velocity to the oxidizer flow and produce a strong swirling motion to the combustion chamber. This improves oxidizer-fuel mixing, flame anchoring, and convective heat transfer to the fuel grain surface. Experimental studies have shown that swirl injectors lead to significantly higher regression rates than conventional showerhead injectors [28] while numerical optimisation studies have suggested that stable combustion is achieved for swirl numbers S between 0.6 and 0.9 [29]. The swirl number is given by:

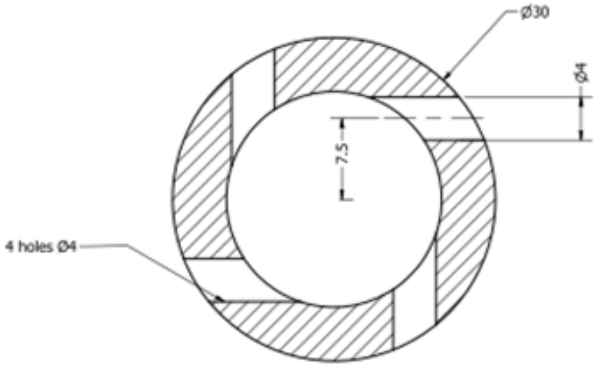
$$S = \frac{G_\phi R}{G_x} \tag{1}$$

where:

$$\begin{aligned} G_\phi &= \text{axial flux of tangential momentum} \\ G_x &= \text{axial flux of axial momentum} \\ R &= \text{characteristic radius (typically chamber or port radius)} \end{aligned}$$

The swirl injector employed in the present work(Figure 3) consists of a cylindrical swirl chamber with four tangential inlet ports (diameter 1.5 mm each), a swirl chamber diameter of 8 mm and a central outlet orifice of diameter 4 mm. The tangential ports are uniformly distributed along the circumference to guarantee axisymmetric swirling flow and the swirl number is 0.7 ($S = 0.7$). The injector is stainless steel and mounted in the forward closure of the motor.

During operation, gaseous oxygen (GOX) enters through the tangential ports, gains a high angular velocity, and exits through the central orifice into the combustion chamber, producing a strong vortex that persists along the entire length of the swirl-star fuel grain.



(a) Schematic cross-section with key dimensions (tangential port: 4×1.5 mm, swirl chamber: 8 mm, outlet orifice: 4 mm).



(b) 3D part of stainless steel swirl injector.

Figure 3: Swirl injector used in all tests.

2.3 Test Setup and Throttling Mechanism

The experimental of test rig was constructed for steady-state characterization and active throttling operation. Fig. 4 shows a schematic of the fluid delivery and control architecture. The test stand with the modified hybrid rocket motor installed. Throttling is done with the dual-line oxidizer manifold (in yellow), with a separate nitrogen purge line used for fast post-shutdown cooling and dependable flame-out. The gaseous oxygen (GOX) supply system consisted of a high-pressure storage tank (main tank), a pressure regulator to reduce the delivery pressure to $\sim$ 20 bar, and a precision mass flow controller (MFC) which could control flow rates up to 36 g/s with an accuracy of $\pm 1\%$ of reading.

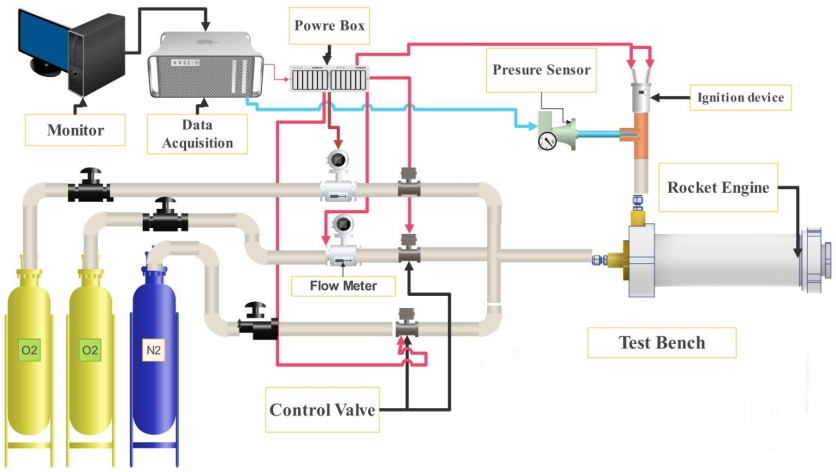


Figure 4: Experimental test setup for the steady state and active throttling test.

2.3.1 Throttling Architecture — Dual-Line Oxidizer Delivery

A dual-line parallel-path oxidizer delivery system was employed to allow for rapid, repeatable transitions between boost and throttling concepts of [21, 6] are employed to maintain thrust levels. The system consisted of two flow paths,

each controlled independently:

1. **Primary (Boost) Line:** This line provided the 5 g/s of oxidizer flow rate for steady state and 2.5 g/s of flow rate for the high thrust boost phase during throttling tests. The line on/off was operated using a normally-closed high-speed solenoid valve.
2. **Secondary (Sustain) Line:** This line was configured with a reduced flow rate of 2.5 g/s for the low thrust sustain phase. This preset flow rate was kept constant by a separate solenoid valve and needle valve combination.

2.3.2 Throttling Sequence and Valve Logic

The throttling procedure for dual-thrust testing was performed as follows:

- **Ignition (t = 0 s):** The boost and sustain solenoid valves were opened simultaneously and the entire 5 g/s was introduced into the combustion chamber. Combustion was started by firing the igniter charge simultaneously.
- **Boost Phase (t = 0.4 to 4 s):** Both valves were opened and the oxidizer flow was kept constant at 5 g/s. The motor was in its usual high-pressure state.
- **Throttling Transition (t = 4 to 4.5 s):** The boost-line solenoid valve was closed by a transistor–transistor logic (TTL) command signal from the data acquisition system, while the sustain-line valve was kept open. The oxidizer flow was suddenly reduced from 5 g/s to 2.5 g/s.
- **Sustain Phase (t = 4.5 to 9.5 s):** The motor was run at the reduced flow rate, and the chamber pressure was adapted to the new equilibrium condition imposed by the regression law of the grain.
- **Shut-off (t = 9.5 to 10 s):** The valve keeping the sustain-line open was closed and the flow of the oxidizer was stopped; the test was ended.

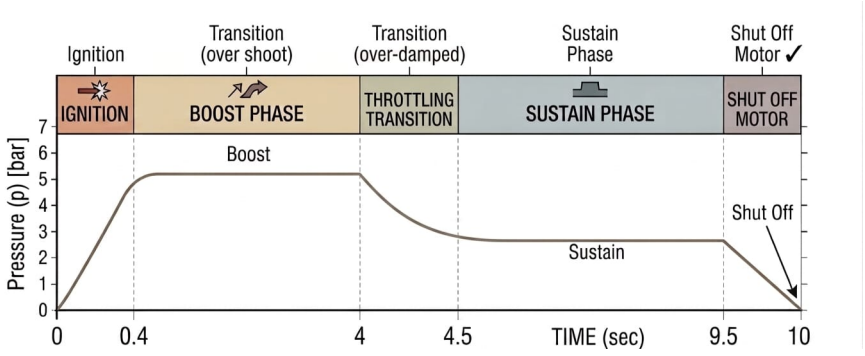


Figure 5: Throttling description.

TThis parallel-path approach reduces the response time of conventional single-valve throttling where the valve partially closes and rests in an intermediate position. The step change is practically instantaneous relative the thermal time constants of the motor.

Ignition was achieved by using a small solid propellant charge (HTPB/AP) ignited by a heated Kanthal wire. The exam uses two oxidizer feed lines for throttling tests and one feed line for mono-thrust operation. A committed Nitrogen cylinder is used for post shutdown cooling and purging.

2.3.3 Instrumentation and Data Acquisition

The experimental control architecture consists of six critical elements to ensure accurate parametric control and procedural repeatability. The primary system pressure is damped by a reduction valve and calibrated mass flow controllers [37] govern precise propellant feed rates. High-fidelity pressure transducers [38] allow continuous data real-time system monitoring and acquisition. Electromagnetically activated solenoid valves [39], direct system isolation and automated flow sequencing are achieved with hand operated valves [40] are used for automated flow sequencing and system isolation. This mixing of hardware (activated by an igniter that provides the required activation energy) can significantly reduce the variance of the experiments, thus providing the ultra-stable conditions required for accurate ballistic data acquisition.The chamber pressure was recorded using a pressure transducer (range 0–100 bar, accuracy ±0.25

2.4 Test Matrix

A complete test matrix was performed as summarized in Table 2. The study included 60 static fire tests with varying grain design (TB, 5SSR, 5SSR f0.3, 7BS, 7SS, 7SSR, 9SSR) and burn time (4, 7, 10 s). Each test condition was repeated at least twice to ensure statistical significance. Additionally, 6 throttling tests were carried out on star grains with $N = 5, 7, 9$ (see Table 3) to specifically assess the dual-thrust transition behaviour. This increases the total number of tests to 66 experiments.

Table 2: Test matrix of steady state firing tests.

Burn time	**TB**	**5SSR**	**5SSR f0.3**	**7BS**	**7SS**	**7SSR**	**9SSR**
4 s	3	3	2	3	3	3	3
7 s	3	3	2	3	3	3	3
10 s	3	3	2	3	3	3	3

Note: Values indicate number of test repetitions. 5SSR f0.3 indicates a 5-point star-swirl-reverse with 0.3 mm fillet (rounded corners). 7BS = 7-point basic star. 7SS = 7-point swirl star. 7SSR = 7-point swirl star reverse. Total runs: 60.

Table 3: Throttling test matrix for dual-throttling evaluation.

Grain	**Test duration (s)**	**Boost duration (s)**	**Sustain duration (s)**	**Boost $\dot{m}_{ox}$ (g/s)**	**Sustain $\dot{m}_{ox}$ (g/s)**	**Repeats**
5SS	10	5	5	5	2.5	2
7SS	10	5	5	5	2.5	2
9SS	10	5	5	5	2.5	2

2.5 Data Reduction Methodology

The average regression rate $\bar{r}$ was calculated from the mass loss of the fuel grain using the following expression [8, 9]:

$$\bar{r} = \frac{\Delta m_f}{\rho \, \bar{A}_b \, t_b} \tag{2}$$

where $\Delta m_f = m_i - m_f$ is the consumed fuel mass, ρ is the measured density of the printed ABS ($1.04\,\mathrm{g\,cm^{-3}}$), t_b is the total burn time, and $\bar{A}_b$ is the average burning surface area over the combustion duration. For complex internal geometries such as swirl-star ports, the instantaneous burning surface area $A_b(t)$ evolves nonlinearly due to the

regression of multiple star points and swirl channels. Therefore, the use of an arithmetic average $\bar{A}_b = (A_{b,i} + A_{b,f})/2$ introduces a systematic uncertainty that is commonly accepted in hybrid rocket literature when instantaneous regression measurements are unavailable [24].

The average oxidizer mass flux $\bar{G}_{\text{ox}}$ was calculated as:

$$\bar{G}_{\text{ox}} = \frac{\dot{m}_{ox}}{\bar{A}_{port}} \tag{3}$$

where $\dot{m}_{ox}$ is the constant oxidizer mass flow rate (controlled by the MFC with an accuracy of ±1% of reading), and $\bar{A}_{port}$ is the average port cross-sectional area. The latter was determined from the average port diameter $\bar{D} = (D_i + D_f)/2$, assuming a circular equivalent port area for simplicity, acknowledging that the swirl-star geometry deviates from a perfect circle [6].

Values used for data reduction of all tests are listed in Appendix A. The regression rate law $\bar{r} = a\bar{G}_{\text{ox}}^{n}$ was fitted to the experimental data using a least-squares regression on the log-transformed variables:

$$\ln(\bar{r}) = \ln(a) + n\ln(\bar{G}_{\text{ox}}) \tag{4}$$

The coefficient a and the exponent n were determined for each grain configuration (tubular, 5SSR, 7BS, 7SS, 7SSR, 9SSR) using the averaged data points from repeated tests at three burn times (4, 7, and 10 seconds). The goodness of fit was evaluated using the coefficient of determination R^2.

For throttling operation, the average chamber pressure is evaluated separately for the two quasi-steady combustion phases (boost and sustain), as given by

$$P_{c,\text{ave,QS1}} = \frac{1}{t_{\text{QS1}}} \int_{t_{\text{QS1}}} P_c(t)\, dt \tag{5}$$

$$P_{c,\text{ave,QS2}} = \frac{1}{t_{\text{QS2}}} \int_{t_{\text{QS2}}} P_c(t)\, dt \tag{6}$$

3 Results and Discussion

In this work, additively manufactured fuel grains were used to improve the regression rate and mass flux in hybrid rocket motors. The study used a baseline 3D-printed tubular grain and then adopted the swirl injector which demonstrated better performance as compared to the showerhead design. The geometry was then evolved to a star shaped port which greatly improved the regression behaviour. The SSR design showed better combustion characteristics from the studied configurations (basic, swirl and swirl star reverse).

A parametric study (N = 5, 7 and 9) showed that N = 5 provided the highest regression rate but also yielded an undesired combustion exponent ($n > 1$). In contrast, the 7SSR configuration presented a balanced performance with a relatively high regression rate and stable combustion behaviour ($n < 1$), and thus was selected as the optimal design.

These findings were used to investigate the throttling performance of star geometries (N = 5, 7 and 9). The results showed that complex star based geometries, especially the SSR design, provided better control of the regression rate and mass flux in throttled operation, leading to better ballistic performance and thrust modulation capability.

3.1 Steady-State Regression Properties

Figure 6 summarizes the steady state regression behavior for all grain configurations tested. This is due to the port area increasing with burn time and the G_{ox} decreasing accordingly. This is a well known trend in hybrid rocket literature [8, 9]. The standard deviation of $\bar{r}$ over repeated tests was typically 5–7

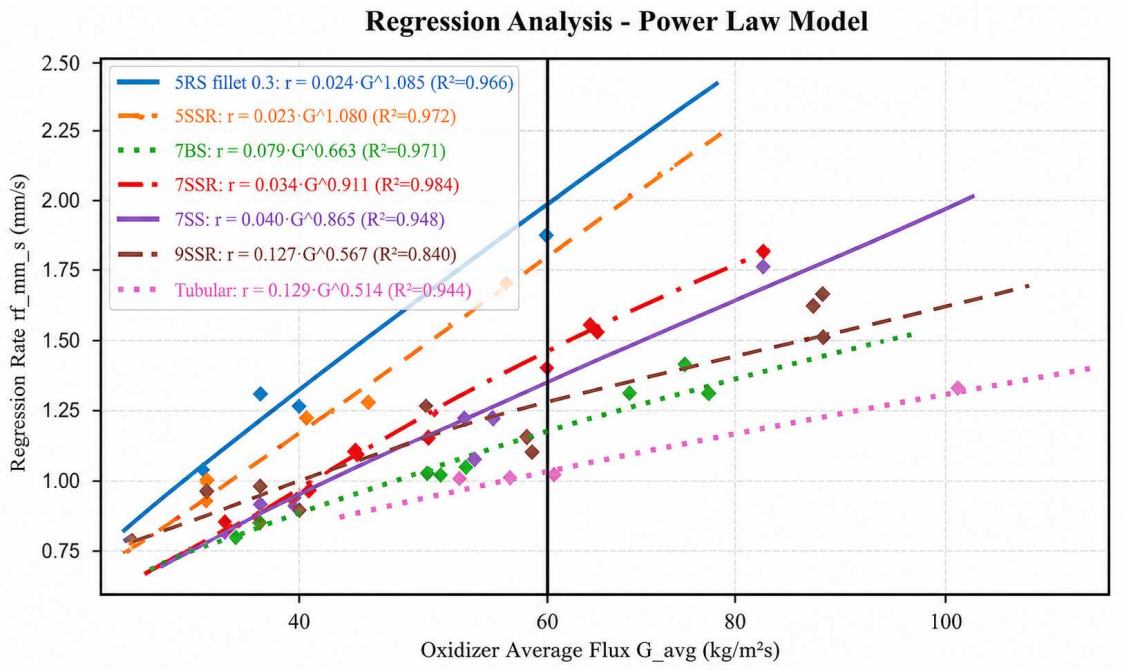


Figure 6: Assembly curve for all steady state regression rate.

TThe empirical regression rate laws are listed in Table 4 and demonstrate a clear trend of a linear oxidizer-flux dependence for increasingly aggressive grain swirling. The tubular geometry gives $n = 0.617$ in good agreement with classical diffusion-limited theory. The basic 7-point star (7BS) provides the exponent with a small boost to 0.663. The introduction of swirl (7SS) increases n to 0.865, while the reverse-twist version (7SSR) retains a high exponent of 0.911 but offers a superior trade-off between coefficient a and exponent. The largest exponent > 1 ($n = 1.080$) is obtained for the 5-point SSR grain at the expense of a smaller coefficient and a possible geometrical instability. The 9-point SSR grain regresses with $n = 0.567$. The regression rate was evaluated at a fixed oxidizer mass flux $G_{ox} = 60$ kg/(m^{2}s) for comparison between grain geometries. The values obtained, presented in the last column of Table 4, represent a direct reference for tubular and star-shaped grain configurations, approaching the behavior of a cylindrical port, when the star points are too numerous to maintain a strong vortex. These observations are in good agreement with recent observations on swirl-enhanced combustion [30] and the review on innovative grain designs [31]. Furthermore, the ballistic performance of these complex geometries has been demonstrated to be highly sensitive to the port features [14].

The results confirm that the SSR geometry changes the heat-transfer mechanism from diffusion-dominated to convection-dominated. An exponent close to unity is highly desirable for throttling applications, because it improves the tracking of the commanded oxidizer flow with the fuel gasification, minimizing drift and improving the dynamic response.

Table 4: Regression rate laws for all tested configurations.

Grain type	a	n	**Regression rate** $\dot{r} = aG_{ox}^n$	R^2	$\dot{r}$ @ $G_{ox} = 60$ **kg/(m^{2}s)** (mm/s)
5SSR f0.3	0.0244	1.085	$\dot{r} = 0.0244\, G_{ox}^{1.085}$	0.966	2.00
5SSR	0.0230	1.080	$\dot{r} = 0.0230\, G_{ox}^{1.080}$	0.972	1.78
7SSR	0.0396	0.911	$\dot{r} = 0.0396\, G_{ox}^{0.911}$	0.984	1.45
7SS	0.0342	0.865	$\dot{r} = 0.0342\, G_{ox}^{0.865}$	0.948	1.30
9SSR	0.1213	0.567	$\dot{r} = 0.1213\, G_{ox}^{0.567}$	0.861	1.27
7BS	0.0787	0.663	$\dot{r} = 0.0787\, G_{ox}^{0.663}$	0.971	1.20
TB	0.0820	0.617	$\dot{r} = 0.0820\, G_{ox}^{0.617}$	0.967	1.05

Based on the above, while the 5-point swirl grains maximise raw regression rates, their exponents critically exceed unity ($n > 1$), risking severe oxidizer-to-fuel ratio shifts. Because stable hybrid rocket combustion strictly requires a mass flux exponent below unity ($n < 1$), the 7-point configurations (7SS and 7SSR) emerge as the optimal design space. Crucially, this underscores the fundamental advantage of additive manufacturing: by enabling the fabrication of complex 3D-printed swirl geometries, it allows researchers to precisely manipulate internal flow dynamics, successfully resolving the trade-off between maximised fuel regression and reliable, steady-state combustion.

3.2 Throttling and Dual-Thrust Performance

This section analyses the dual-throttling response of the swirl star reverse (SSR) grains as illustrated in Figure 7. The repeatability is essential for establishing confidence in the throttling metrics (settling time, undershoot magnitude) extracted from the pressure traces. Figure 8 shows throttling test results for two repeated tests of SSR grains. A repeatable 8–10% pressure undershoot is evident due to reduced oxidizer flow and fuel thermal lag, with boosting from 0.4–4.00 s at 5.00 g/s, transition from 4.00–4.5 s, and sustain from 4.5–9.0 s at 2.5 g/s followed finally by rapid shut-off from 9.5–10 s. The near-perfect overlay of repeats confirms deterministic undershoot rather than instability.

Having validated the test methodology, we now compare the throttling response across the three SSR grain configurations. Figures 7 and 8 present the chamber pressure histories for the remaining throttling tests.

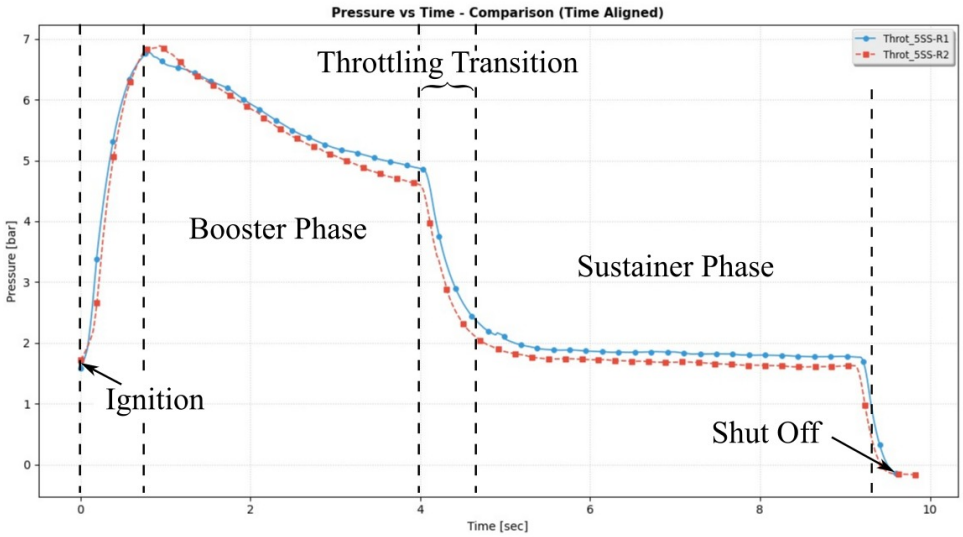


Figure 7: Timeline for throttling experiments.

The pressure–time curve for 5SSR as shown in Figure 8 shows a clear boost–sustain transition at $t \approx 5$ s, followed by a pressure overshoot and oscillatory decay. This indicates strong but unstable coupling between oxidizer flux and regression rate due to geometry-induced vortex sensitivity, limiting throttling stability. The 7SSR configuration exhibits a smooth and rapid transition from the boost to the sustain phase with minimal undershoot and no oscillations. This reflects a near-linear coupling between oxidizer flux and regression rate, enabling stable and well-controlled throttling. Finally, the 9SSR curve shows a gradual pressure decay after throttling, indicating an intermediate transition to the sustain phase.

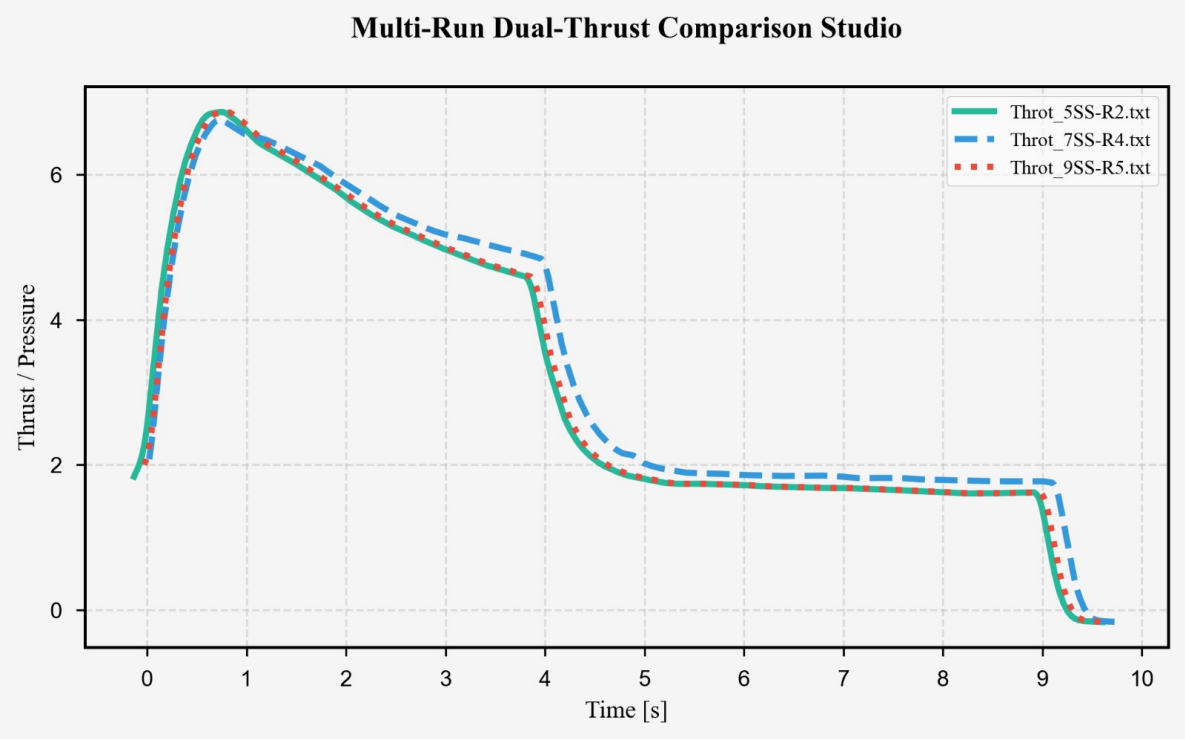


Figure 8: Pressure-time curve for throttling swirl star grain at $N = 5, 7, 9$. The response is sluggish for 9SSR, indicative of a weak regression-flux coupling.

The throttling behaviour of the swirl star reverse grains as described above is summarised in Table 5. The 5SSR grain ($n = 1.080$) exhibits an oscillatory response with a transient pressure spike and a moderate transition time of 0.62 s, indicating sensitivity to rapid flow variations due to unstable vortex structures. In contrast, the 7SSR configuration ($n = 0.911$) demonstrates the most stable and responsive behaviour, achieving a slightly longer but well-controlled transition (0.87 s) with minimal undershoot ($< 5\%$) and no oscillations, reflecting optimal coupling between oxidizer flux and fuel regression. The 9SSR grain ($n = 0.567$) shows a slower dynamic response despite a nominal transition time of 0.64 s, as the weak dependence of regression on the oxidizer flux leads to a gradual pressure decay and reduced throttling precision.

Table 5: Impact of transition time between boost and sustain phases.

Grain Type	$\mathbf{P}_{\text{boost}}$ (bar)	$\mathbf{P}_{\text{sustain}}$ (bar)	$\mathbf{t}_{\text{transition}}$ (s)
5SSR	9.312	6.007	0.62
7SSR	9.433	5.988	0.87
9SSR	9.332	5.856	0.64

4 Conclusion

This experimental study has systematically characterized the steady-state regression and the dynamic throttling behavior of additively manufactured ABS fuel grains with tubular, swirl-star and star-swirled reverse port geometries coupled with a swirl injector. The experimental results have shown that additive manufacturing is a promising approach for hybrid rocket throttling applications. By designing the internal port geometry, a stable, high intensity swirl can be maintained even at lower oxidizer flow rates. This results in a more linear motor response. This greatly facilitates the design of closed loop controllers. Instead of having to compensate for a highly non-linear hysteretic plant, the control system can deal with a more predictable actuator. Further testing at larger scales is needed, but the lack of

significant pressure oscillations during step transients within the limits of these small-scale tests indicates a reduced risk of combustion instability.

From a mission design perspective, the 2:1 throttling ratio (5 to 2.5g/s) demonstrated boost-sustain capability as a proof of concept for larger motors, but deeper throttling ratios will be required for applications such as planetary landing. A 7SSR grain together with a digital throttle valve array, as proposed by Whitmore [21], could allow precise thrust profiles for missions that transition from a high thrust braking phase to a low thrust hover phase. The thermoplastic ABS fuel brings the logistic advantage of its on-demand printability, which is a key enabler for in-situ resource utilisation (ISRU) concepts [32]. Conclusions are based on 66 static fire tests, including 6 specific experiments on active throttling:

The 7-point swirl-star-reverse (7SSR) grain among the tested configurations gives the most favourable combination of high regression exponent ($n = 0.865$) and stable transient response. This grain shows a clean boost-sustain transition with a pressure undershoot of less than 5

Regarding the trade-off in extreme geometries, the 5-point SSR grain has the highest exponent ($n = 1.080$) but shows oscillatory pressure behaviour during throttling due to the unstable vortex structures induced by the sharp star tips. In contrast, the 9-point SSR grain returns to a low exponent (n = 0.575) and a sluggish pressure response (stabilisation time ≈ 2 s). The excess of star points here inhibits sustained swirl, so the grain behaves effectively as a circular port.

Validation of the dual-line throttling architecture demonstrates that the parallel solenoid valve system provided repeatable, near-instantaneous step transitions as indicated by the close overlay of pressure traces from repeated tests. This hardware approach, together with high-n fuel grain, enables a practical realisation of programmable thrust profiles without complex feedback compensation. The use of time-averaged burning surface area $barA_b$ introduces a systematic uncertainty (estimated as $pm5\%$ for $barr$) and the assumption of uniform axial regression must be validated by CT-based reconstruction or multi-port instrumentation.

Additionally, the present study is limited to a throttling ratio of 2:1 (5 to 2.5 g/s) and a single motor scale (1-inch). Extrapolation to larger motors or deeper throttling ratios should be exercised with caution. The combination of additive manufacturing with swirl injection and the optimized 7SSR geometry provides a new design paradigm for throttleable hybrid rockets. Future work should include (i) scaling the demonstrated concept to thrust levels of interest for orbital manoeuvring and planetary landing (e.g. 500-5000 N), (ii) adding energetic additives (e.g. aluminium or copper compounds) to increase the pre-exponential factor a while keeping $n \approx 0.865$, (iii) developing model-based closed-loop controllers utilizing the near-linear response, and (iv) studying the long-duration regression behaviour and thermal management in sustain-phase operation.

In conclusion, this study provides empirical regression laws and transient throttling data for additively manufactured swirl-star grains, demonstrating that the 7SSR configuration can be operated responsively with low oscillation in dual-thrust. These results provide a foundation for future hybrid propulsion systems with programmable thrust profiles including multi-pulse orbital transfer vehicles, precision landers, and guided missiles.

A Appendix A

Table 6: Parameters used for data reduction.

Test	t (s)	m_i (g)	m_f (g)	l_i (mm)	l_f (mm)	D_i (mm)	D_f (mm)	$\bar{r}$ (mm/s)	$\bar{G}_{ox}$ (kg/m^{2}s)
TB-R1	3.81	105.7	100.3	50.12	46.40	4.65	11.24	1.39	100.8
TB-R2	3.63	107.4	100.2	50.02	46.58	4.65	10.95	1.38	104.6
TB-R3	3.66	107.3	100.8	49.76	46.12	4.65	11.01	1.42	103.7
TB-R4	6.83	108.4	91.40	50.00	44.25	4.65	14.51	1.13	69.3
TB-R5	6.80	105.4	94.40	50.07	43.59	4.65	15.72	1.10	61.3
TB-R6	6.81	105.1	98.10	49.73	43.25	4.65	14.25	1.11	71.2
TB-R7	9.72	108.0	92.00	50.07	41.42	4.65	16.97	0.91	54.4
TB-R8	9.53	107.7	92.80	49.80	40.06	4.65	17.80	0.89	52.4
TB-R9	9.72	108.8	92.00	49.87	39.47	4.65	7.98	0.91	49.7

Table 6 (continued)

Test	t (s)	m_i (g)	m_f (g)	l_i (mm)	l_f (mm)	D_i (mm)	D_f (mm)	$\bar{r}$ (mm/s)	$\bar{G}_{ox}$ (kg/m^{2}s)
5SSR-R1	3.78	103.6	93.0	50.08	44.94	4.86	15.82	1.83	59.50
5SSR-R2	3.68	105.5	95.0	50.13	45.35	4.86	16.06	1.84	58.10
5SSR-R3	3.88	105.6	94.8	50.21	45.43	4.86	16.32	1.76	56.73
5SSR-R4	6.82	105.5	89.7	50.06	42.80	4.86	19.50	1.27	42.86
5SSR-R5	6.82	103.7	88.0	49.98	41.96	4.86	19.23	1.28	43.83
5SSR-R6	6.89	97.8	82.0	50.04	42.57	4.86	18.77	1.30	45.56
5SSR-R7	9.90	100.7	81.4	49.85	41.30	4.86	21.47	0.99	36.69
5SSR-R8	9.98	99.8	78.7	49.79	39.54	4.86	22.85	1.02	33.12
5SSR-R9	9.90	105.1	83.8	50.16	38.60	4.86	22.64	1.05	33.64
5SSRf-R1	3.69	105.1	94.2	50.14	45.98	4.86	16.04	1.91	58.21
5SSRf-R2	3.63	102.3	91.2	50.02	45.77	4.86	16.57	1.92	55.39
5SSRf-R3	6.82	103.1	86.8	50.08	42.73	4.86	20.12	1.28	40.78
5SSRf-R4	6.64	97.3	80.3	49.86	42.25	4.86	20.76	1.34	38.76
5SSRf-R5	9.82	102.1	81.2	49.86	40.51	4.86	22.57	1.04	33.82
5SSRf-R6	9.97	105.3	83.5	50.09	39.16	4.86	23.05	1.05	32.67
7BS-R1	3.87	105.0	98.0	50.06	47.03	4.84	13.31	1.34	77.23
7BS-R2	3.86	105.6	97.9	50.03	45.67	4.84	13.15	1.49	78.61
7BS-R3	3.90	106.7	99.2	49.77	46.34	4.84	13.47	1.40	75.92
7BS-R4	6.88	106.4	94.5	50.10	43.36	4.84	15.99	1.12	58.66
7BS-R5	6.87	107.5	95.7	49.82	44.58	4.84	15.50	1.14	61.50
7BS-R6	6.89	106.0	94.2	49.76	43.52	4.84	15.56	1.12	61.13
7BS-R7	9.89	108.0	90.9	50.07	40.58	4.84	19.32	0.96	43.59
7BS-R8	9.88	108.2	91.6	50.03	41.17	4.84	19.68	0.92	42.32
7BS-R9	9.89	106.7	90.2	49.83	40.38	4.84	19.59	0.91	42.65
7SS-R1	3.86	105.7	97.0	50.09	46.84	4.65	13.80	1.63	74.30
7SS-R2	3.86	107.4	98.6	50.06	46.26	4.65	14.05	1.64	72.70
7SS-R3	3.90	107.3	98.3	50.13	46.74	4.65	14.50	1.61	69.40
7SS-R4	6.84	108.4	95.2	50.05	43.09	4.65	16.70	1.22	55.57
7SS-R5	6.87	105.4	91.9	50.01	44.40	4.65	18.00	1.16	49.30
7SS-R6	6.89	105.1	91.3	49.79	43.99	4.65	18.17	1.17	48.90
7SS-R7	9.89	108.0	90.4	50.06	40.80	4.65	20.80	0.94	39.18
7SS-R8	9.88	107.7	89.7	50.09	41.20	4.65	19.30	1.02	44.32
7SS-R9	9.89	108.8	91.0	50.07	40.80	4.65	19.85	0.98	42.39
7SSR-R1	3.94	105.9	96.5	49.88	46.84	4.84	13.19	1.68	70.54
7SSR-R2	3.78	106.5	97.3	49.80	46.27	4.84	13.09	1.71	69.39
7SSR-R3	3.85	101.9	92.7	49.76	46.75	4.84	13.10	1.66	68.78
7SSR-R4	6.83	100.0	86.8	50.01	43.10	4.84	16.31	1.20	53.86
7SSR-R5	6.87	107.1	95.1	50.05	44.40	4.84	16.60	1.09	54.54
7SSR-R6	6.92	102.7	88.9	49.91	43.99	4.84	16.72	1.22	53.15
7SSR-R7	9.88	107.2	89.6	50.02	40.88	4.84	20.55	0.96	41.10
7SSR-R8	9.86	101.7	83.5	50.10	41.21	4.84	21.54	0.98	39.94
7SSR-R9	9.86	106.4	88.3	49.96	40.80	4.84	21.33	0.98	40.20
9SSR-R1	3.84	105.3	97.8	50.10	46.16	4.86	12.66	1.51	82.82
9SSR-R2	3.80	105.1	97.0	50.13	46.32	4.86	13.29	1.59	81.62
9SSR-R3	3.78	106.4	98.1	50.04	46.15	4.86	12.97	1.65	80.04
9SSR-R4	6.71	100.2	86.2	50.20	43.56	4.86	16.93	1.28	53.58
9SSR-R5	6.57	108.0	96.1	49.84	43.60	4.86	15.37	1.20	62.18
9SSR-R6	6.81	106.1	94.3	50.14	45.33	4.86	15.42	1.14	61.84
9SSR-R7	9.67	105.9	89.3	49.79	41.58	4.86	19.08	0.96	44.37
9SSR-R8	9.66	99.2	79.3	49.87	40.72	4.86	21.81	1.03	35.77
9SSR-R9	9.93	100.1	80.5	50.06	38.25	4.86	20.73	1.03	38.84

Acknowledgements

The authors gratefully acknowledge the support of the Military Technical College, Egypt, for providing the experimental facilities and funding for this research.

Funding

This research did not receive funding.

Data Availability

Data and analysis scripts are available from the corresponding author upon reasonable request.

Author Contributions Statement

M.E. conceived the experiments and conducted the test campaign; A.F.A. Hassan designed the fuel grains and injectors; A.H. supervised the experimental work and analysed the data; M.Y.M.A. performed the data reduction and drafted the manuscript. All authors reviewed and approved the final version.

Competing Interests

The authors declare no competing interests.

References

[1] Wei, X. et al. Review of hybrid rocket propulsion. *Progress in Aerospace Sciences* **142**, 100957 (2024).

[2] Mane, S. & Kumar, R. Advancements in hybrid rocket motors. *Journal of Propulsion and Power* **39**, 210–225 (2023).

[3] Altman, D. & Holzman, A. Hybrid rocket development. *AIAA Journal* **29**, 2162–2167 (1991).

[4] Karp, A. et al. Hybrid rocket propulsion for small satellites. *Acta Astronautica* **202**, 124–136 (2023).

[5] Carmicino, C. & Sorge, A. Influence of a conical axial injector on hybrid rocket performance. *Journal of Propulsion and Power* **22**, 984–991 (2006).

[6] Whitmore, S. et al. Closed-loop control of 3D-printed hybrid rockets. *Journal of Propulsion and Power* **30**, 1522–1531 (2014).

[7] Marxman, G. & Gilbert, M. Turbulent boundary layer combustion in the hybrid rocket. In *Ninth Symposium (International) on Combustion*, 371–383 (1963).

[8] Kuo, K. K. & Chiaverini, M. J. (eds.) *Fundamentals of Hybrid Rocket Combustion and Propulsion*, Progress in Astronautics and Aeronautics, Vol. 218 (AIAA, 2007).

[9] Altman, D. Overview of hybrid rocket propulsion. In Kuo, K. K. & Chiaverini, M. J. (eds.) *Fundamentals of Hybrid Rocket Combustion and Propulsion*, 1–16 (AIAA, 2007).

[10] Oztan, C. & Coverstone, V. 3D printing of hybrid rocket fuels. *Additive Manufacturing* **38**, 101823 (2021).

[11] Paravan, C. et al. Combustion of 3D-printed hybrid rocket fuel grains. *Acta Astronautica* **159**, 205–216 (2019).

[12] Armold, D. et al. Test of 3D-printed fuel grains for hybrid rockets. In *49th AIAA/ASME/SAE/ASEE Joint Propulsion Conference*, AIAA 2013-3876 (2013).

[13] Modechang, S. et al. Study of star-swirl ABS grains in hybrid rockets. *Combustion and Flame* **262**, 113456 (2025).

[14] Hashish, A. et al. Ballistic performance of armored grains for vortex flow pancake motors. In *AIAA Propulsion and Energy Forum*, AIAA 2023-2345 (2023).

[15] Liu, Y. et al. Fuel grain with star-swirl configuration and swirl injector. *Aerospace Science and Technology* **150**, 109321 (2025).

[16] Heydari, M. et al. Experimental investigation of swirling oxidizer flow in HTPB/N2O motors. *Journal of Propulsion and Power* **33**, 1445–1453 (2017).

[17] Funami, R. et al. Regression rate of star-fractal swirl ports. In *AIAA Propulsion and Energy Forum*, AIAA 2023-4567 (2023).

[18] Takano, S. et al. System demonstration of star-fractal swirl hybrid rocket. *Acta Astronautica* **215**, 234–245 (2024).

[19] Wang, Z. et al. Combustion of swirl-radial-injection composite grains. *Combustion and Flame* **248**, 112578 (2023).

[20] El-Naggar, M., Ayad, A. F., Hashish, A. & Ahmed, M. Y. M. Experimental investigation of 3D-printed tubular and swirl star grains as solid fuels for hybrid rocket engines. (2025).

[21] Whitmore, S. & Walker, S. Development of digital throttling for hybrid rockets. *Journal of Propulsion and Power* **40**, 112–123 (2024).

[22] Ruffin, A. et al. Real-time deep throttling using cavitating venturis. In *AIAA Propulsion and Energy Forum*, AIAA 2022-3987 (2022).

[23] Dinesh, K. et al. Demonstration of passive dual-thrust modulation. *Acta Astronautica* **218**, 123–134 (2024).

[24] Wei, X. et al. Experiment and internal ballistic reconstruction for hybrid rockets. *Aerospace Science and Technology* **136**, 108223 (2023).

[25] Whitmore, S. et al. Analytical ballistic consistency of 3D-printed ABS. *Journal of Propulsion and Power* **27**, 1050–1058 (2011).

[26] Whitmore, S. et al. Test of copper-infused 3D-printed ABS in hybrid rockets. *Journal of Propulsion and Power* **37**, 567–578 (2021).

[27] Gallo, M. et al. Prediction of regression rate for HDPE/nitrous oxide hybrids. *Journal of Propulsion and Power* **40**, 289–298 (2024).

[28] Bouziane, M. et al. Experimental comparison of injectors for hybrid rockets. *Acta Astronautica* **152**, 734–742 (2018).

[29] Tian, H. et al. Numerical optimization of hybrid rocket injector and chamber. *Aerospace Science and Technology* **128**, 107756 (2022).

[30] Stella, F. et al. Experimental investigation of swirl-enhanced hybrid rockets. *Journal of Propulsion and Power* **40**, 421–434 (2024).

[31] Santolini, A. et al. Innovative fuel grain designs for hybrid rockets. *Aerospace Science and Technology* **145**, 108876 (2024).

[32] Aqailan, M. et al. Vortex cooling in 3D-printed thermoplastic chambers. *Additive Manufacturing* **78**, 103856 (2025).

[33] Prusa Research. Prusa Website. https://www.prusa3d.com/ (2022). Accessed: 2022-03-22.

[34] Bisin, R., Paravan, C., Alberti, S. & Galfetti, L. A new strategy for the reinforcement of paraffin-based fuels based on cellular structures: The armored grain—mechanical characterization. *Acta Astronautica* **176**, 494–509 (2020).

[35] Bisin, R., Verga, A., Bruschi, D. & Paravan, C. Strategies for paraffin-based fuels reinforcement: 3D printing and blending with polymers. In *AIAA Propulsion and Energy 2021 Forum* (2021).

[36] Bisin, R. *3D printed cellular structures for solid fuel grains: perspectives for enhanced mechanical and ballistic performance of paraffin-based fuels*. PhD thesis, Politecnico di Milano (2022).

[37] Bronkhorst. Bronkhorst Website. https://www.bronkhorst.com/int/ (2022). Accessed: 2022-01-12.

[38] HBM. HBM Website. https://www.hbm.com/it/ (2022). Accessed: 2022-03-10.

[39] PeterPaul. PeterPaul Website. https://peterpaul.com/ (2022). Accessed: 2022-05-25.

[40] Swagelok. Swagelok valves: tubing and hand valves. https://products.swagelok.com/en/all-products/valves/c/200 (2022). Accessed: 2022-03-22.

[41] National Instruments. PXI systems and data acquisition (DAQ) solutions. https://www.ni.com/en/shop/hardware-portfolio/pxi.html (2022). Accessed: 2022-03-22.